# Anomalous Near-Field Heat Transfer between a Cylinder and a Perforated Surface

Alejandro W. Rodriguez,[1,2] M. T. Homer Reid,[2] Jaime Varela,[3] John D. Joannopoulos,[4] Federico Capasso,[1] and Steven G. Johnson[2]

[1]*School of Engineering and Applied Sciences, Harvard University, Cambridge, Massachusetts 02138, USA*
[2]*Department of Mathematics, Massachusetts Institute of Technology, Cambridge, Massachusetts 02139, USA*
[3]*Department of Physics, University of California Berkeley, Berkeley, California 94704, USA*
[4]*Department of Physics, Massachusetts Institute of Technology, Cambridge, Massachusetts 02139, USA*

(Received 12 July 2012; published 2 January 2013)

We predict that the near-field radiative heat-transfer rate between a cylinder and a perforated surface depends nonmonotonically on their separation. This anomalous behavior, which arises due to evanescent-wave effects, is explained using a heuristic model based on the interaction of a dipole with a plate. We show that nonmonotonicity depends not only on geometry and temperature but also on material dispersion—for micron and submicron objects, nonmonotonicity is present in polar dielectrics but absent in metals with small skin depths.

DOI: 10.1103/PhysRevLett.110.014301 PACS numbers: 44.40.+a, 05.70.Ln, 12.20.−m

Disconnected bodies of unequal temperatures can exchange energy through stochastic electromagnetic waves [1–8], a phenomenon known as radiative heat transfer that underlies many naturally occurring and technologically relevant processes [7,8]. Recent advances in microfabrication and metrology have enabled experiments that can now regularly probe this phenomenon at micron and submicron scales [9,10]. At such small scales, unusual near-field interactions arise [8], but nonplanar geometries in this context are only just beginning to be explored [11–23]. In this Letter, inspired by our previous work on Casimir repulsion [24], we demonstrate that the near-field heat transfer between a cylinder (or elongated object) and a perforated surface (e.g., a ring) can vary nonmonotonically with respect to their mutual separation. This anomalous effect stems primarily from the contribution of dipolar fields, as illustrated by a heuristic model in which the cylinder is modeled as a quasistatic dipole and the ring as an infinitesimally thin plate with a hole. We find that nonmonotonicity weakens (eventually disappearing) whenever the geometrical and material parameters of the objects deviate significantly from the dipolar regime: for cylinders of nearly equal aspect ratio, large ring thicknesses, large temperatures, or metals with small skin depths (such as gold), the usual monotonic dependence is observed. Our calculations reveal that, in contrast to more conventional geometries, ''additive'' approximations such as the well-known proximity approximation cannot predict this effect, even qualitatively.

In the far field (object separations $d$ much greater than the thermal wavelength $\lambda_T = \hbar c/k_B T$), radiative heat transfer is dominated by the exchange of propagating waves and is thus nearly insensitive to changes in separations (oscillations from interference effects typically beings small [1,25]). In the (less studied) near field ($d \lesssim \lambda_T$), not only are interference effects important, but otherwise-negligible evanescent waves also contribute flux [7,8]. Such near-field effects have been most commonly studied in planar geometries, where the monotonically increasing contribution of evanescent waves with decreasing $d$ results in orders-of-magnitude enhancement of the net radiative heat-transfer rate (exceeding the far-field blackbody limit at submicron separations [8]). Consequently, the net radiative heat-transfer rate between objects in the near field usually increases monotonically with decreasing $d$, with only a few exceptions. Nonmonotonic changes have been predicted to occur in the shallow ($d \sim \lambda_T$) and deep ($d \ll$ object sizes $\ll \lambda_T$) near-field regimes due to interference of propagating waves and atomic-scale phenomena. For instance, deviations from monotonicity on the order of 10% have been predicted (and even experimentally observed [26]) in the plate–plate [1] and nanoparticle–plate [25] geometries at several microns separations, just as near-field contributions begin to play a significant role. Even larger deviations have been predicted to occur at nano and subnanometer separations [8,27], where macroscopic electromagnetism breaks down. Thus far, however, little is known about the near-field heat-transfer characteristics of bodies whose shapes differ significantly from the planar, unpatterned structures of the past, leaving open the possibility of geometrically induced ($d \sim$ object sizes) nonmonotonicity dominated by near-field ($d \ll \lambda_T$) effects. Recent theoretical progress along these lines include predictions for a handful of new geometries, including spheres [11,18] and cones [19] suspended above slabs, as well as patterned surfaces [12–16,20]. In what follows, we describe a situation in which near-field interactions mediated by evanescent waves cause large nonmontonic changes in the net heat-transfer rate between micron-scale bodies at separations ($d \sim$ hundreds of nanometers) comparable to the object sizes.

The heat-transfer rate $H$ between two objects held at temperatures $T_1$ and $T_2$ can be expressed in the form [1,7,8]

 

$$H = \int_0^\infty d\omega[\Theta(\omega, T_2) - \Theta(\omega, T_1)]\Phi(\omega), \qquad (1)$$

where $\Phi$ is the flux spectrum (the time-averaged flux into object 2 due to current sources in object 1), and $\Theta(\omega, T) = \hbar\omega/[\exp(\hbar\omega/k_B T) - 1]$ is the mean Planck energy per oscillator at frequency $\omega$ and temperature $T$. (Note that $\Phi = 1$ for blackbodies that capture all of one another's radiation.) We compute $\Phi$ by exploiting two recent computational methods: a fluctuating surface-current (FSC) formulation involving the solution of an integral equation at each frequency [22], and a Langevin finite-difference time-domain (FDTD) formulation in which one explicitly time-evolves Maxwell's equations in response to (broad-bandwidth) stochastic sources inside the bodies [15]. In order to distinguish the effects of geometry from those of material dispersion, we begin by considering a simple model material: a lossy dielectric with a broad (low-dispersion) absorption peak, given by $\varepsilon(\omega) = \varepsilon_\infty - \sigma/(\omega_0^2 - \omega^2 - i\gamma\omega)$, with $\varepsilon_\infty = 12.5$, $\sigma = 4 \times 10^2$ $(c/\mu\text{m})^2$, $\omega_0 = 0$, and $\gamma = 60$ $(c/\mu\text{m})$, corresponding to roughly constant $\text{Re}\varepsilon \approx 12$ and large $\text{Im}\varepsilon \gtrsim 1$ over relevant frequencies. Later, we consider realistic materials and show that material dispersion also plays a crucial role.

We previously studied the radiation of isolated cylinders and rings [22]. Here, we consider the new phenomena that arise when these objects are brought into close proximity so that near-field effects are present. The dashed green lines in the inset of Fig. 1 show the flux spectrum of an isolated cylinder ($\Phi_c$) of radius $R = 0.1$ $\mu$m and aspect ratio $\Lambda = L/2R = 5$, and of an isolated ring ($\Phi_r$) of outer (inner) diameter $D = 2$ $\mu$m ($W = 0.8$ $\mu$m) and thickness $h = 0.05D$, as a function of frequency (units of $2R/\lambda$). In this long-wavelength limit ($\lambda \gg R$), large $\text{Im}\varepsilon$ and the absence of geometric and material resonances means that both objects emit significantly less than an ideal blackbody, with ($\Phi_c \ll \Phi_r \ll 1$).

The inset in Fig. 1 also shows the flux spectrum $\Phi$ when the two objects are brought into close proximity (solid lines), at three different center-center separations $d$, showing dramatic changes from the isolated case. $\Phi$ is computed via both FDTD (noisy curves) and FSC (smooth curves) methods, showing excellent agreement; the remaining calculations use FSC only. Compared to isolated objects, the increasing contribution of evanescent waves in both objects leads to an overall increase in the flux at low frequencies. [Note that the peak in $\Phi$ at $\lambda \approx 10^{-3}R$ is a consequence of material dispersion: the loss tangent of the material $\sim \text{Im}\varepsilon/\text{Re}\varepsilon \to \infty$ as $\lambda \to \infty$, leading to zero radiation; the peak in the spectrum occurs at the crossover wavelength for which $\text{Im}\varepsilon \sim \text{Re}\varepsilon$. Low-frequency cutoffs in the near-field enhancement occur in highly conductive materials, such as gold (below).] Most interestingly, however, the enhancement in $\Phi$ here does not increase monotonically with decreasing $d$: $\Phi$ increases from $d = \infty$ to $d \approx 0.4L$ but decreases from $d \approx 0.4L$ to $d = 0$.

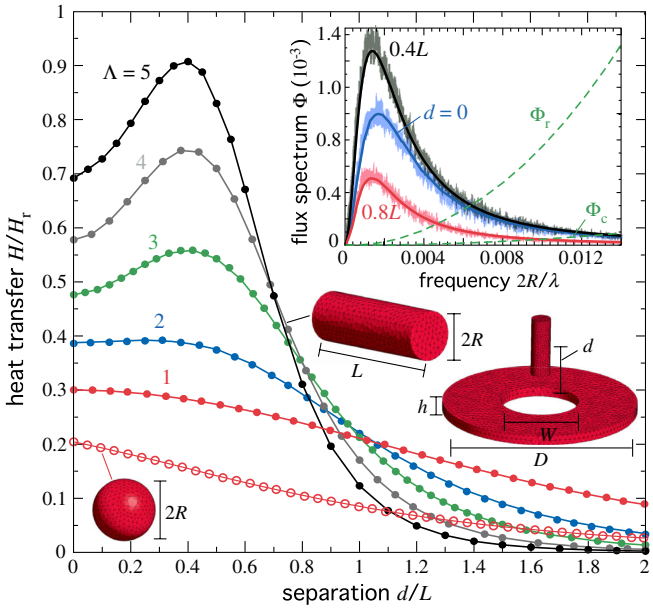


FIG. 1 (color online). Heat-transfer rate $H$ from a room-temperature ring to a cylinder (or sphere) of fixed radius $R = 0.1$ $\mu$m and aspect ratio $\Lambda = L/2R$ held at $T = 0$, as a function of their center-center separation $d$. $H$ is normalized by the heat radiation of the isolated ring $H_r$. Both objects are lossy dielectrics with $\text{Re}\varepsilon \approx 12$ (see text). Inset shows the flux spectrum $\Phi(\omega)$ of the $\Lambda = 5$ configuration at three separations, and also of the isolated cylinder and ring (dashed lines).

To explore the geometry dependence of this near-field behavior, we now examine the overall heat-transfer rate $H$ as a function of $d$ instead of the spectrum. In particular, Fig. 1 shows $H$ from a room-temperature ring to a cylinder at $T = 0$, for multiple aspect ratios $\Lambda$. For comparison, $H$ is normalized to the radiation rate of the isolated ring $H_r$. For large anisotropy $\Lambda = 5$, $H$ first increases as the two objects approach each other due to the usual near-field enhancement and then decreases as $d \to 0$, peaking at a critical separation $d_c \approx 0.4L$. Unlike previously studied structures involving noninterleaved objects, the heat transfer in this geometry does not diverge as $d \to 0$: although the two objects approach each other in this limit, they never touch. Also, $H \to 0$ as $d \to \infty$ due to the finite size of the two objects. As $\Lambda$ decreases (keeping $R$ fixed), corresponding to increasingly isotropic cylinders, the nonmonotonicity becomes less pronounced and is completely absent in both the $\Lambda = 1$ configuration (small anisotropy) and for a sphere (open red circles). As expected, there is an overall decrease in $H$ with decreasing $L$ due to the decreasing volume of the cylinder. Nonmonotonicity also slowly disappears as the ring thickness $h$ increases to $h \approx 0.5L$, leaving a relatively wide range of thicknesses over which the effect can be observed. Furthermore, as expected, the strength of the nonmonotonicity $H(d_c)/H(0)$ grows larger as the cylinder surface approaches the rim of the ring (corresponding to larger $R$ or smaller $W$) due to usual near-field effects, and

also for larger $D$ due to the larger surface area. We also find that nonmonotonicity persists even when the cylinders are shifted laterally (shifts $<0.5W$), an asymmetric configuration that is likely to occur in experiments. Finally, we find that $H(d_c)/H(0)$ increases as $h, R, L \to 0$ (for fixed $\Lambda$), as seen below (Fig. 2).

Cylindrical symmetry allows us to decompose $\Phi$ into azimuthal angular components $m$ (fields $\sim e^{im\theta}$), implemented in FDTD with cylindrical coordinates. Our calculations reveal (not shown) that most (though not all) of the nonmonotonic dependence comes from the contribution of dipolar ($m = 0$) fields, which dominate the heat transfer at these long thermal wavelengths $\lambda_T \gg R, L$. At such $\lambda$, a cylinder with large $\Lambda$ will act like a fluctuating dipole oriented mainly along the symmetry axis of the ring—strictly speaking, this is true only for separations $\gg R, L$. Since the fields generated by a fluctuating dipole are polarized mostly along the dipole axis and since current fluctuations in the thin ring are polarized mostly along the plane of the ring, it follows that the fields induced by a long $z$-oriented cylinder will do less work on currents in the ring whenever the objects are nearly coplanar ($d \to 0$).

We quantify this argument by focusing on a simple (albeit heuristic) model in which the cylinder is modeled as a dipole of electric polarizability $\boldsymbol{\alpha}^E(\omega)$ and the ring as an infinitesimally thin plate with a hole. For convenience, we only consider the nonretarded (quasistatic) limit of small dipole separations $d \ll \lambda_T$, in which case the heat-transfer rate between the dipole and plate can be expressed as $H_d = \int d\omega[\Theta(\omega, T_1) - \Theta(\omega, T_2)]\Phi_d(\omega)$, where the flux spectrum is given by [6,28,29]

$$\Phi_d(\omega) = \frac{2}{\pi}\sum_i \omega^2 \mathrm{Im}[\alpha_i^E(\omega)]\mathrm{Im}[G_{ii}(\mathbf{r}_d, \mathbf{r}_d)]. \qquad (2)$$

Here, $G_{ij}(\mathbf{r}, \mathbf{r}')$ is the electric Green's function of the plate—the electric field in the $i$th direction at $\mathbf{r}$ due to a dipole source in the $j$th direction at $\mathbf{r}'$—and $\mathbf{r}_d$ is the location of the dipole. The calculation of $G_{ij}$ for a perfectly conducting, infinitely thin plate was carried out in Ref. [30] for the purpose of computing the Casimir-Polder force in that idealized system. However, because perfect conductors do not radiate ($\mathrm{Im}G_{ij} = 0$), we merely exploit that expression as the starting point of a quasistatic perturbative calculation in which the plate is assumed to have a small amount of absorption. In particular, we are interested in computing the dissipated power or Ohmic losses on a plate with small but finite conductivity $\sigma$, given the quasistatic fields at the surface of the perfectly conducting plate. Following Ref. [31], the resistive losses on the plate are $\sim \mathrm{Im}G_{jj}(\mathbf{r}_d, \mathbf{r}_d) \sim \int d^2\mathbf{r}\sigma(\mathbf{r})|\mathbf{G}_j^0(\mathbf{r}, \mathbf{r}_d)|^2$, where $G_{ij}^0$ is the electric Dyadic Green's function of the unperturbed (perfectly conducting) plate, and the integral is performed over the plate surface. It turns out that $G^0$ exhibits nonintegrable singularities at the rim of the hole, a well-known artifact of the idealized nature of corners and wedges in electromagnetism [31]. While the electromagnetic energy corresponding to these fields is finite when integrated over all space, the singularity in the fields is problematic for the perturbation theory since the form of the perturbation considered here requires that $G^0$ be integrated only over the plane of the plate. Essentially, this model does not account for the finite thickness of the plate, and consequently fails to capture effects associated with the finite penetration or skin-depth $\delta = c/(\omega\mathrm{Im}\sqrt{\varepsilon})$ of fields. Therefore, we use $\delta$ as a cutoff length scale to regularize the integral near the rim of the hole. Surprisingly, and despite its many shortcomings, this heuristic model captures most of the features of interest.

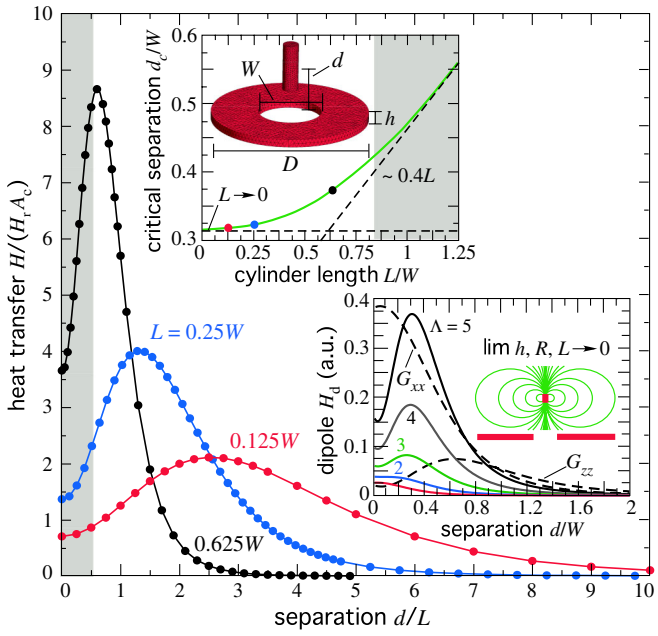


FIG. 2 (color online). Heat-transfer rate $H$ between the ring and cylinder of Fig. 1, for fixed cylinder aspect ratio $\Lambda = 5$ and thin ring thickness $h = 5 \times 10^{-3}D$, as a function of $d$ and for multiple cylinder lengths $L$. $H$ is normalized by the radiation of the isolated ring $H_r$ multiplied by the cylinder area $A_c$. The shaded region denotes separations over which the two objects are interleaved. Top inset shows the critical separation $d_c$ of largest $H$ as a function of $L$, with shaded areas again denoting interleaved configurations. Bottom inset shows $H$ (solid lines) along with $\mathrm{Im}G_{ii}$ at the cylinder location (dashed lines) in the limit $h, R, L \to 0$, as computed by a heuristic model (see text).

The bottom inset in Fig. 2 shows the computed $\mathrm{Im}G_{ii}$ and resulting heat-transfer rate $H_d$ (in arbitrary units) from a room-temperature plate of conductivity $\sigma = \omega\mathrm{Im}\varepsilon$, infinitesimally small thickness $h \to 0$, and hole diameter $W$, to a small cylinder of radius $R \ll W$ and electric polarizability $\boldsymbol{\alpha}^E$ held at $T = 0$, as a function of their separation $d$. $H_d$ is computed by Eq. (2) using the dipole model above, with the polarizability of the dipole taken to be that of a uniform prolate spheroid [29] of aspect ratio $\Lambda = L/2R$ and permittivity $\varepsilon$ (same as above). At large $d \gg W$, the presence of the hole in the plate is negligible and hence

$\mathrm{Im}G_{ii} \to 0$ in the usual monotonic fashion [31]. At small $d \lesssim W$, the hole dramatically alters the interaction, making it highly orientation dependent: $\mathrm{Im}G_{zz}$ is nonmonotonic with $d$, achieving its maximum at $d \sim W$, whereas $\mathrm{Im}G_{xx}$ is strictly monotonically increasing with decreasing $d$. Essentially, the electric field lines of $z$- and $x$-oriented dipoles lie mostly perpendicular and parallel to the plate, respectively, leading to weaker and stronger interactions as $d \to 0$. Since $\mathrm{Im}G_{zz} \ll \mathrm{Im}G_{xx}$ at separations $d \lesssim W$, it follows that $H_d$ will become nonmonotonic at large enough anisotropies $\Lambda$ (equivalently, for $\alpha_z^E/\alpha_x^E \gg 1$). For $\Lambda = 5$, corresponding to a highly anisotropic object, one observes the expected nonmonotonic behavior, with the critical separation $d_c \approx 0.3W$ determined by $W$. As before, nonmonotonicity decreases with decreasing $\Lambda$, disappearing completely in the limit $\Lambda \to 1$ of an isotropic (spherical) object with polarizability $\alpha^E = 4/3\pi R^3(\varepsilon - 1)/(\varepsilon + 2)$. In comparison with Fig. 1, we observe that the simple model quantitatively captures the onset of nonmonotonicity at $\Lambda \gtrsim 2$. Since the model represents a point-dipole limit, we also compare to exact calculations for fixed $\Lambda = 5$ by letting $L \to 0$ and $h = 5 \times 10^{-3}D$, as shown in Fig. 2. While nonmonotonicity is present for all $L$, the scaling of the critical separation $d_c$ with $L$ changes qualitatively as $L \to 0$. Specifically, as shown by the top inset of Fig. 2, $d_c \approx 0.3W$ for $L \ll W$, in *quantitative* agreement with the dipole model, while $d_c \approx 0.4L$ for $L \gg W$, with the crossover regime occurring at $L \approx 0.5W$. We find that for $L \lesssim 0.8W$, the onset of nonmonotonicity ($d_c$) occurs before the two objects are interleaved, i.e., when there is a separating plane between the objects.

Aside from geometry, changes coming from either temperature or material dispersion leading to deviations from the ideal dipole regime can also weaken nonmonotonic behavior. Thus far, we have restricted ourselves to studying microscale bodies near room temperature (which emit preferentially at infrared frequencies), corresponding to large thermal wavelengths $\lambda_T \gg R$. At larger temperatures ($\lambda_T \lesssim R$), however, such bodies can no longer be well described as dipole emitters, and thus $\Phi$ no longer exhibits nonmonotonic behavior. We find that nonmonotonicity persists at temperatures well beyond the mere $T \approx 300$ K considered here, so long as the feature sizes of the objects involved remain at or below the micron scale. Realistic materials often exhibit substantial material dispersion at or near infrared wavelengths, and this can also significantly alter the dipole picture above. This situation is depicted in Fig. 3, which shows $H$ for various material configurations, including metals (gold and indium tin oxide) and polar dielectrics (doped silicon). (The Au and ITO dispersions are determined by Drude models with plasma frequencies $\omega_p = 1.367 \times 10^{16}$ rad/s and $\omega_p = 1.4739 \times 10^{15}$ rad/s and relaxation rates $\gamma = 5.317 \times 10^{13}$ rad/s and $\gamma = 1.5347 \times 10^{14}$ rad/s, respectively, whereas the doped silicon dispersion is given by the model of Ref. [32].)

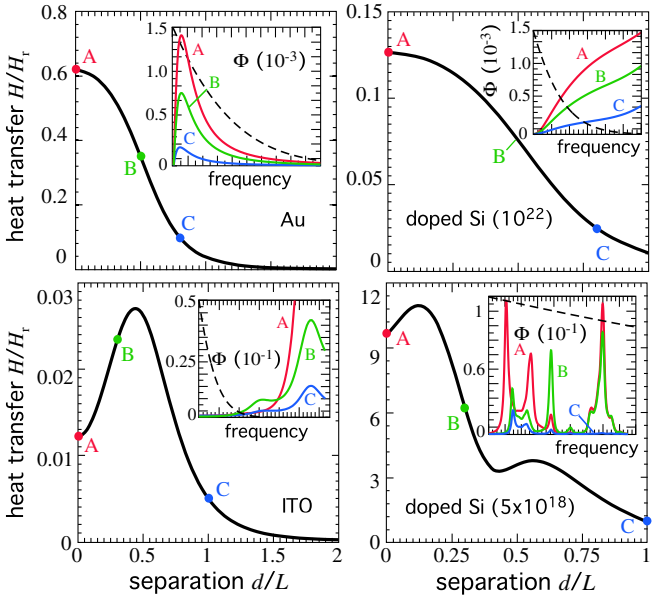


FIG. 3 (color online). Heat-transfer rate $H$ between the ring and cylinder of Fig. 1, for fixed cylinder aspect ratio $\Lambda = 5$, as a function of separation $d$. $H$ is normalized to the radiation rate of the isolated ring $H_r$, and plotted for multiple material configurations. Insets show the corresponding flux spectra $\Phi(\omega)$ at three different (labeled) separations.

Interestingly, we find that nonmonotonicity is completely absent for the Au and highly doped silicon ($10^{22}$ cm$^{-3}$) configurations and present in the ITO and lesser-doped silicon ($5 \times 10^{18}$ cm$^{-3}$) configurations. The reason for the discrepancy comes from the fact that highly conductive metals and polar dielectrics respond very differently to incident light. In particular, for metals, the electric dipole approximation (above) breaks down for skin depths $\delta \ll R, L$: in that limit, eddy currents induced on the surface of the metallic objects also lead to large magnetic dipole moments [28,29,33], with magnetic polarizabilities $\boldsymbol{\alpha}^H \gg \boldsymbol{\alpha}^E$. Unfortunately, the interaction between a magnetic dipole moment and a plate does not exhibit the desired nonmonotonic effect (at least in this geometry), which explains the results in the case of Au and highly doped silicon cylinders, whose skin depths $\delta \approx 10^{-2}$ $\mu$m $\ll R$ at infrared wavelengths. If we scale the entire structure down to much smaller scales $R, L \ll \delta$ (not shown), we find that nonmonotonicity is restored. Thus, for highly conductive materials, one obtains the desired nonmonotonic effect only for $h, R, L \ll \delta \ll \lambda_T$.

The insets in Fig. 3 show the flux spectra of the various material configurations at three separations (labeled $A$, $B$, and $C$), along with normalized plots of the mean Planck energy per oscillator at room temperature (dashed lines), showing the various frequency contributions. The Au and highly doped silicon $\Phi$ are monotonic with $d$ at all frequencies. On the other hand, ITO and lesser-doped silicon are nonmonotonic with $d$ only at certain frequencies. For any material, $\Phi$ is monotonic at high frequencies

($\lambda \ll R, L$), where the cylinder no longer acts as a dipole, but this transition occurs even more rapidly for ITO (which is only nonmonotonic for low frequencies) because of the aforementioned skin-depth effect. For silicon, the situation is greatly complicated by the presence of multiple geometric resonances ($\varepsilon$ has a single absorption peak), arising from the ability of the fields to probe the interior as well as the surface of the dielectric. It turns out that only two of the resonant peaks in this case exhibit nonmonotonicity with $d$, corresponding to resonances with the necessary dipolelike polarizations.

Similar and even more pronounced nonmonotonic behaviors should arise in other geometries, so long as the suspended objects (regardless of shape) are sufficiently anisotropic (behave dipolelike) and radiate primarily in the direction orthogonal to the patterned surface. An interesting structure to explore in the future is a nanowire array suspended above a periodically patterned thin film.

This work was supported by DARPA Contract No. N66001-09-1-2070-DOD and by the AFOSR Multidisciplinary Research Program of the University Research Initiative (MURI) for Complex and Robust On-chip Nanophotonics, Grant No. FA9550-09-1-0704.

[1] D. Polder and M. Van Hove, Phys. Rev. B **4**, 3303 (1971).
[2] S. M. Rytov, V. I. Tatarskii, and Y. A. Kravtsov, *Principles of Statistical Radiophsics II: Correlation Theory of Random Processes* (Springer-Verlag, Berlin, 1989).
[3] J.-P. Mulet, K. Joulain, R. Carminati, and J.-J. Greffet, Microscale Therm. Eng. **6**, 209 (2002).
[4] K. Joulain, J.-P. Mulet, F. Marquier, R. Carminati, and J.-J. Greffet, Surf. Sci. Rep. **57**, 59 (2005).
[5] V. P. Carey, G. Cheng, C. Grigoropoulos, M. Kaviany, and A. Majumdar, Nanoscale Micro. Thermophys. Eng. **12**, 1 (2008).
[6] A. I. Volokitin and B. N. J. Persson, Rev. Mod. Phys. **79**, 1291 (2007).
[7] Z. M. Zhang, *Nano/Microscale Heat Transfer* (McGraw-Hill, New York, 2007).
[8] S. Basu, Z. M. Zhang, and C. J. Fu, Int. J. Energy Res. **33**, 1203 (2009).
[9] E. Rousseau, A. Siria, J. Guillaume, S. Volz, F. Comin, J. Chevrier, and J.-J. Greffet, Nat. Photonics **3**, 514 (2009).
[10] S. Shen, A. Narayanaswamy, and G. Chen, Nano Lett. **9**, 2909 (2009).
[11] A. Narayanaswamy and G. Chen, Phys. Rev. B **77**, 075125 (2008).
[12] S.-A. Biehs, O. Huth, and F. Ruting, Phys. Rev. B **78**, 085414 (2008).
[13] G. Bimonte, Phys. Rev. A **80**, 042102 (2009).
[14] R. Messina and M. Antezza, Phys. Rev. A **84**, 042102 (2011).
[15] A. W. Rodriguez, O. Ilic, P. Bermel, I. Celanovic, J. D. Joannopoulos, M. Soljacic, and S. G. Johnson, Phys. Rev. Lett. **107**, 114302 (2011).
[16] M. Kruger, T. Emig, and M. Kardar, Phys. Rev. Lett. **106**, 210404 (2011).
[17] P. Ben-Abdallah, S.-A. Biehs, and K. Joulain, Phys. Rev. Lett. **107**, 114301 (2011).
[18] C. Otey and S. Fan, Phys. Rev. B **84** 245431 (2011).
[19] A. P. McCauley, M. T. H. Reid, M. Kruger, and S. G. Johnson, Phys. Rev. B **85**, 165104 (2012).
[20] J. Lussange, R. Guérout, F. S. S. Rosa, J. J. Greffet, A. Lambrecht, and S. Reynaud, Phys. Rev. B **86**, 085432 (2012).
[21] R. Guèrout, J. Lussange, F. S. S. Rosa, J. P. Hugonin, D. A. R. Dalvit, J. J. Greffet, A. Lambrecht, and S. Reynaud, Phys. Rev. B **85**, 180301 (2012).
[22] A. W. Rodriguez, M. T. H. Reid, and S. G. Johnson, Phys. Rev. B **86**, 220302(R) (2012).
[23] S. A. Biehs, M. Tschikin, and P. Ben-Abdallah, Phys. Rev. Lett. **109**, 104301 (2012).
[24] M. Levin, A. P. McCauley, A. W. Rodriguez, M. T. Homer Reid, and S. G. Johnson, Phys. Rev. Lett. **105**, 090403 (2010).
[25] M. Tschikin, S. A. Biehs, F. S. S. Rosa, and P. B. Abdallah, Eur. Phys. J. B **85**, 233 (2012).
[26] C. M. Hargreaves, Phys. Lett. **30**, 491 (1969).
[27] A. Perez-Madrid, L. C. Lapas, and J. M. Rubi, Phys. Rev. Lett. **103**, 048301 (2009).
[28] P.-O. Chapuis, M. Laroche, S. Volz, and J.-J. Greffet, Phys. Rev. B **77**, 125402 (2008).
[29] O. Huth, F. Ruting, S.-A. Biehs, and M. Holthaus, Eur. Phys. J. Appl. Phys. **50**, 10603 (2010).
[30] C. Eberlein and R. Zietal, Phys. Rev. A **83**, 052514 (2011).
[31] J. D. Jackson, *Classical Electrodynamics* (Wiley, New York, 1998), 3rd ed.
[32] L. Duraffourg and P. Andreucci, Phys. Lett. A **359**, 406 (2006).
[33] E. A. Garcia, R. Gomez-Medina, L. S. Froufe-Perez, C. L. Lopez, F. Scheffold, J. Aizpurua, M. Nieto-Versperina, and J. J. Saenz, Opt. Express **19**, 4815 (2011).